Clim. Past Discuss., 5, 1297–1336, 2009
www.clim-past-discuss.net/5/1297/2009/


*Climate of the Past Discussions* is the access reviewed discussion forum of *Climate of the Past*

# Warm Paleocene/Eocene climate as simulated in ECHAM5/MPI-OM

**M. Heinemann**[1,2], **J. H. Jungclaus**[1], **and J. Marotzke**[1]

[1]Max Planck Institute for Meteorology (MPI-M), Hamburg, Germany
[2]International Max Planck Research School on Earth System Modelling (IMPRS-ESM), Hamburg, Germany

Received: 7 April 2009 – Accepted: 27 April 2009 – Published: 5 May 2009

Correspondence to: M. Heinemann (malte.heinemann@zmaw.de)

Published by Copernicus Publications on behalf of the European Geosciences Union.

## Abstract

We investigate the late Paleocene/early Eocene (PE) climate using the coupled atmosphere-ocean-sea ice model ECHAM5/MPI-OM. The surface in our PE control simulation is on average 297 K warm and ice-free, despite a moderate $CO_2$ concentration of 560 ppm. Compared to a pre-industrial reference simulation (PR), low latitudes are 5 to 8 K warmer, while high latitudes are up to 40 K warmer. This high-latitude amplification is in line with proxy data, yet a comparison to sea surface temperature proxy data suggests that the Arctic surface temperatures are still too low.

To identify the mechanisms that cause the PE-PR temperature difference, we fit a zero-dimensional energy balance model to the ECHAM5/MPI-OM results. Doubled $pCO_2$ in PE compared to PR, increased atmospheric water vapour, and a slightly increased longwave cloud radiative forcing together cause about 2/3 of the PE-PR temperature difference; planetary albedo changes cause about 1/3. Our results support the hypothesis that local radiative effects as well as topographic changes, rather than increased meridional heat transports, were responsible for the "equable" PE climate.

## 1 Introduction

Simulating warm periods in Earth history is a major challenge in climate research. The very warm climates during the late Cretaceous to early Paleogene (about 100 to 35 million years ago) seem especially problematic, since model results are not consistent with paleo-reconstructions of low pole-to-equator temperature gradients and reduced seasonalities on high-latitude continents.

In this study, we aim at reducing this gap between modelling and proxy data for the late Paleocene/early Eocene (PE), about 55 million years ago. To this end, we set up a PE version of the coupled atmosphere-ocean-sea ice general circulation model (GCM) ECHAM5/MPI-OM. Using a simple energy balance model, we quantify the mechanisms that lead to the warm climate in our PE GCM.



CPD

5, 1297–1336, 2009



Evidence for the warm PE climate is provided by a wide range of proxies. Sea surface temperatures (SSTs) inferred from oxygen isotopes, Mg/Ca ratios, and biomarkers suggest that the tropics were moderately warmer than at present, while high latitudes and especially Arctic temperatures were much warmer (e.g., Thomas et al., 2002; Tripati and Elderfield, 2004; Zachos et al., 2003, 2006; Sluijs et al., 2006). Estes and Hutchinson (1980) found warm-climate proxies such as salamanders, lizards, snakes, turtles, and an alligator on the Canadian Archipelago (see also Markwick, 1994, 1998). Greenwood and Scott (1995) inferred from the existence of high-latitude palm trees that a large part of the Earth surface, including continental interiors, had climates with winter temperatures much higher than today.

Climate models, employing large greenhouse gas concentrations, have been able to reproduce the high mean temperature of the PE (e.g., Shellito et al., 2003). However, it has long been noticed that they fail to match the low pole-to-equator temperature gradient (e.g., Barron, 1987). Note that, when Barron (1987) discussed the low pole-to-equator temperature gradient problem, it was believed that tropical SSTs during the PE were even lower than at present (e.g., Shackleton and Boersma, 1981). This led Barron (1987) to the conclusion that "the Eocene polar warmth could be explained by an energy redistribution, a more efficient poleward heat transport, and external factors would be not required". Ever since, tropical temperature reconstructions have been adjusted towards warmer conditions (e.g., Sexton et al., 2006). If very high tropical temperatures are confirmed by further proxy analyses, the mismatch between models and proxy data may be reduced further (Huber, 2008).

Taking the warm poles, relatively cold tropics, and reduced seasonality at face value, it has been suggested that the climate models lack one or more mechanisms that lead to such a so-called "equable" climate. Increased ocean heat transport has often been invoked to explain the problematic warm poles (e.g., Covey and Barron, 1988). Sloan et al. (1995) estimated that a 30% increase in poleward heat transport would be required to maintain Eocene high-latitude temperatures. Huber and Sloan (2001) revisited the hypothesis of increased oceanic heat transport, and simulated the Eocene

with a fully coupled atmosphere-ocean-sea ice GCM, the Climate System Model (CSM) version 1 developed at the National Center for Atmospheric Research (NCAR). Their Eocene model solution showed a near-modern meridional temperature gradient, and a near-modern oceanic heat transport. They concluded that the theory of increased ocean heat transport for maintaining low temperature gradients was incorrect or incomplete. Other hypotheses draw on local radiative changes rather than heat transport. Sloan and Pollard (1998) suggested that, given high atmospheric methane concentrations, polar stratospheric clouds might contribute to a high-latitude warming. Kump and Pollard (2008) found that increased cloud droplet radii and precipitation efficiency could cause an additional warming and high-latitude amplification. They argued that this change of the cloud properties could have been a response to a reduced global primary production by temperature stress, causing a reduction in cloud condensation nuclei concentration. Abbot and Tziperman (2008) suggested another mechanism related to clouds. They argued that deep convection during winter in ice-free high-latitude oceans might lead to high-latitude warming.

Still, to our knowledge, there is no PE model solution consistent with the geologic record. Modelling the PE remains a major challenge in climate research. We aim at testing whether the model-proxy data mismatch persists in a PE setup of the state-of-the-art coupled model ECHAM5/MPI-OM.

The boundary between the Paleocene and the Eocene is marked by an extraordinary, short-lived global warming event known as the Paleocene/Eocene Thermal Maximum (PETM), also named Late Paleocene Thermal Maximum (LPTM) or Eocene Thermal Maximum 1 (ETM1). This event is associated with a massive increase of atmospheric greenhouse gas concentrations (e.g., Dickens et al., 1995), and is frequently assumed to be an analogue for future greenhouse warming scenarios (e.g., Alley et al., 2002). Note that we aim at modelling the already warm background climate during the PE, not the PETM itself.

To better understand the processes that lead to the warm PE climate in our model, we compare the PE simulation to a pre-industrial reference simulation (PR). We briefly




analyse the atmospheric and oceanic meridional heat transports in the PE model solution compared to PR. However, this study focusses on understanding the radiative effects responsible for the warm PE climate. Using a simple energy balance model, we assign the simulated warming of the PE climate compared to the PR climate to greenhouse gas forcing, albedo changes, cloud feedback processes, orographic effects, and orbital changes.

The paper is organised as follows. In Sect. 2, we describe the atmosphere-ocean-sea ice GCM ECHAM5/MPI-OM, focussing on the settings specific to the PE. In Sect. 3, we describe the simulated PE climate, briefly compare it to the geologic record, and highlight differences compared to PR. In Sect. 4, we analyse the different mechanisms that lead to the warm PE climate in our simulation. In Sect. 5, we present a discussion and conclusions.

## 2 Model setup

Our model ECHAM5/MPI-OM is based on the tropospheric model ECHAM5 resolving the atmosphere up to 10 hPa, the ocean-sea ice model MPI-OM, and the OASIS coupler. In the following section, we describe the basic model properties, boundary conditions, and parameter choices we use in the PE model setup.

### 2.1 Atmosphere general circulation model

The atmosphere general circulation model ECHAM5 (here: version 5.3, Roeckner et al., 2003) has been developed from the operational forecast model of the European Centre for Medium-Range Weather Forecasts (ECMWF) and a parameterisation package developed in Hamburg. ECHAM5 has a spectral dynamical core that solves the equations for vorticity, divergence, temperature and the logarithm of surface pressure in terms of spherical harmonics with a triangular truncation. Transport of water vapour, cloud liquid water, and cloud ice is computed on a Gaussian grid, using a flux-form

semi-Lagrangian scheme (Lin and Rood, 1996). We use the spectral truncation T31, which corresponds to a Gaussian grid with a gridpoint spacing of approximately 3.75°.

The shortwave radiation scheme (Fouquart and Bonnel, 1980) has four spectral bands, one for visible and ultraviolet, and three for the near infrared. The scheme includes Rayleigh scattering, absorption by water vapour, ozone ($O_3$), carbon dioxide ($CO_2$), methane ($CH_4$) and nitrous oxide ($N_2O$). Water vapour is a prognostic variable. Ozone is interpolated in time from a monthly zonal mean climatology (Fortuin and Kelder, 1998). Carbon dioxide, methane and nitrous oxide are assumed to be uniformly mixed. Carbon dioxide estimates for the PE range from 300 ppm to more than 2000 ppm before the PETM, and even higher concentrations during the PETM (Pearson and Palmer, 2000; Royer et al., 2001). Since we aim at simulating the PE background climate, we use a relatively low carbon dioxide concentration of 560 ppm, which is twice the pre-industrial value. There is no proxy available for methane nor for nitrous oxide. For simplicity, methane and nitrous oxide are set to pre-industrial values (concentrations given in Table 1).

Longwave radiation is computed in the Rapid Radiative Transfer Model (RRTM) developed by Mlawer et al. (1997). The RRTM scheme computes fluxes in the spectral range 10 $cm^{-1}$ to 3000 $cm^{-1}$. The computation is organised in 16 spectral bands and includes line absorption by water, carbon dioxide, ozone, methane, nitrous oxide, and aerosols. Aerosol distributions are prescribed following Tanré et al. (1984).

The cloud scheme consists of prognostic equations for water vapour, liquid and solid water, and bulk cloud microphysics. Cloud cover is computed diagnostically from relative humidity following Lohmann and Roeckner (1996).

We interpolate the orography from a 55 Ma 2°×2°geography reconstructed by Bice and Marotzke (2001) (Fig. 1a). The standard version of ECHAM5 utilises a parameterisation developed by Lott and Miller (1997) to account for interactions between subgrid-scale orography (SSO) and the atmospheric flow. This SSO parameterisation needs the standard deviation, anisotropy, slope, orientation, minimum, maximum, and mean elevation of the orography for each gridpoint. Since we do not have that information for



CPD
5, 1297–1336, 2009



the PE, we switch the SSO parameterisation off.

For simplicity, we prescribe a globally homogeneous vegetation (parameters given in Table 1), which is characterised by a lower albedo compared to the PR average, a slightly larger leaf area index, and a larger forest fraction, consistent with a larger fraction of high-latitude, and dark, tropical forests (see, e.g., Utescher and Mosbrugger, 2007, for an Eocene vegetation reconstruction). The leaf area index does not vary seasonally in the PE setup. We prescribe a surface roughness length that resembles the pre-industrial average over land. The soil and vegetation parameter settings are akin a present-day, woody savanna during its growing season (Hagemann et al., 1999; Hagemann, 2002).

River runoff is treated interactively in the atmosphere model, and the respective fresh water flux is passed to the ocean as part of the atmospheric freshwater flux field. In our PE setup, we assume that rivers flow along the geopotential height gradient but overleap valleys such that no lakes are formed.

Orbital parameters in our PE simulation are set to constant values (see Table 1). The longitude of perihelion, the obliquity, and the eccentricity as computed by Laskar et al. (2004) vary on timescales much shorter than the length of the PE period (Fig. 2). Moreover, Laskar et al. (2004) reported that their simulation of the orbital parameters becomes uncertain for more than 40 to 50 Ma ago. We select a longitude of perihelion such that the Northern Hemisphere winter occurs in the aphelion (almost like today). The present-day obliquity and eccentricity are rather extreme values. For the PE, we select an obliquity and an eccentricity closer to the temporal average of the solution by Laskar et al. (2004, see Fig. 2).

### 2.2 Ocean-sea ice general circulation model

The Max-Planck-Institute Ocean Model (MPI-OM, here: version 1.2.0) is a z-coordinate global GCM based on the primitive equations for a hydrostatic Boussinesq fluid with a free surface (Marsland et al., 2003). Scalar and vector variables are formulated on an orthogonal curvilinear C-grid (Arakawa and Lamb, 1977). Along-isopycnal diffusion is

implemented following Griffies (1998). Horizontal tracer mixing by unresolved eddies is parameterised following Gent et al. (1995). For the vertical eddy viscosity and diffusion the Richardson-number dependent scheme of Pacanowski and Philander (1981) is applied. Since the Pacanowski-Philander (PP) scheme in its classical form underestimates the turbulent mixing close to the surface, an additional wind mixing parameterisation is included. In the presence of static instability, convective overturning is parameterised by greatly enhanced vertical diffusion. A bottom boundary layer slope convection scheme allows for an improved representation of the flow of statically unstable dense water over sills. The effect of ocean currents on surface wind stress is accounted for following Luo et al. (2005). The embedded sea ice model consists of sea ice dynamics following Hibler (1979) and zero-dimensional thermodynamics following Semtner (1976). For more details on MPI-OM and the embedded sea ice model see Marsland et al. (2003) and Jungclaus et al. (2006).

To apply MPI-OM to the PE, we include the PE bathymetry and generate an appropriate model grid. As for the orography in the atmospheric model, we interpolate the bathymetry from the reconstruction by Bice and Marotzke (2001). The MPI-OM grid structure allows for an arbitrary placement of the grid poles; we generate a grid with a grid-North Pole on Paleo-Asia and a grid-South Pole on Paleo-South America (Fig. 1b). This model grid has several advantages. Positioning the grid-poles over land removes the numerical singularities associated with the convergence of meridians at the geographical poles. Positioning the grid-poles on *wide* landmasses allows us to reduce the total number of gridpoints. Moreover, this setup yields a higher resolution of many small but important seaways (e.g., open North Atlantic, Central American Seaway, Tethys Seaway, India-Eurasia gateway; Bice and Marotzke, 2002). The grid spacing varies between 70 km around South America and 430 km in the Pacific. We use 40 levels in the vertical, of which 9 levels are in the uppermost 100 meters and 18 levels in the uppermost 500 m.

## 2.3 Spinup

To approach the equilibrium PE climate state, we run the model for 2500 years. The atmosphere and the ocean are initialised at rest. The ocean is initialised at a potential temperature of 283 K, and a salinity of 34.3 psu, which is approximately the salinity we would get in the present-day ocean if all glaciers melted completely. The atmosphere approaches its equilibrium after some 150 years, whereas in most ocean basins the transient phase lasts for about 1000 years. After 1000 years, the globally averaged temperatures even at the deepest levels only increase by less than 0.3 K per 1000 years (Fig. 3).

The Arctic deep ocean takes especially long to equilibrate, since it is only connected to the other basins via shallow sills. Moreover, the Arctic is stratified due to fresh surface water that inhibits vertical mixing. After 2000 years, the Arctic deep ocean is 8 to 10 K warm and still warming by more than 1 K per 1000 years (not shown).

## 2.4 Pre-industrial reference simulation

In this study, we compare the PE simulation to a 2200 year long ECHAM5/MPI-OM simulation with pre-industrial boundary conditions that has been initialised from Levitus data. We refer to this pre-industrial reference simulation as PR. The pre-industrial boundary conditions include the bathymetry, orography, greenhouse gas concentrations, soil and vegetation properties, and orbital parameters (Table 1). The pre-industrial boundary conditions also include the subgrid-scale orographic information; the SSO parameterisation is switched on. Moreover, PR uses a modified physical parameterisation of friction and diffusion to improve the representation of the El Niño-Southern Oscillation (ENSO, see Jungclaus et al., 2006), while PE uses the standard MPI-OM parameter settings as specified by Marsland et al. (2003). While the orbital parameters in PE are constant, the parameters in PR vary temporally according to VSOP87 (Variations Séculaire des Orbites Planétaires, Bretagnon and Francou, 1988). The philosophy behind this approach is to compare the PE simulation to an as good as

possible representation of the pre-industrial climate.

An alternative approach to set up a pre-industrial reference would be to degrade the pre-industrial boundary conditions to the level of accuracy available for the PE (see, e.g., Huber et al., 2003), which would worsen the representation of the pre-industrial climate. Such a degradation would also include to switch off the SSO parameterisation.

To test the effect of the SSO parameterisation, and to ensure that neither the ENSO-tuning nor the dynamic orbital parameters have a major effect on the pre-industrial climate, we perform a 400 year long pre-industrial sensitivity run. This sensitivity run restarts from PR, it does not use the SSO parameterisation nor the ENSO-tuning, and it uses constant orbital parameters as specified in Table 1. Moreover, it uses the PE concentrations of nitrous oxide and methane (Table 1), and a carbon dioxide concentration of 280 ppm (instead of 278 ppm). We find that these differences in the model setup compared to PR lead to a global warming of approximately 0.8 K. The warming is largest at northern high latitudes, where it reaches up to 3 K. However, the differences between this pre-industrial sensitivity run and PR remain small compared to the differences between PE and PR. Using the pre-industrial sensitivity run instead of PR would lead to a small modification of some quantitative results, but the general results and conclusions of this work are not affected.

## 3 Simulated Paleocene/Eocene climate

The aim of this section is to describe the simulated PE climate, to briefly compare it to proxy data, and to identify the main differences between PE and PR.

### 3.1 Surface temperature

The simulated PE Earth's surface is on average 297 K warm and basically ice-free. There is one small area in the Weddell Sea, and one small area north of proto-Greenland that do have a little bit of sea ice in a few, exceptionally cold winters. The

sea ice fraction in these areas amounts to less than 0.1% with a sea ice thickness of less than 3 mm.

The highest annual mean surface temperatures of 313 to 314 K occur in low altitude areas of South Asia, some areas in central South America, and Africa (Fig. 4). During local summers, surface temperatures reach up to 325 K in South Asia, 322 K in central South America, and 318 K in North Africa (temperatures are 200 year means of the warmest month).

The lowest annual mean surface temperatures of about 270 K occur over the Antarctic continent. Antarctic summer surface temperatures are around 295 K even at the coldest places. In the Northern Hemisphere, the lowest surface temperature of 271 K occurs in the Rocky Mountains, where monthly means vary between 261 K and 285 K. The Arctic has the coldest summers on the PE globe; the warmest Arctic monthly mean SSTs only reach about 280 K.

Local winter snow depths reach 1.2 m in the Rocky Mountains, 40 cm in Greenland, 30 cm on the Antarctic continent, and 20 cm in Siberia. During local summers all the snow melts away, there is no long-term snow accumulation.

### 3.2 Comparison to proxy data

We select six different SST reconstructions from the literature to compare them to the simulated zonal mean SSTs (Fig. 5a). We find that five of the six selected SST reconstructions are close to the simulated seasonal variability of the zonal means. One reconstruction differs very much from the simulated zonal mean SST: Sluijs et al. (2006) inferred Arctic SSTs of about 291 K from the biomarker $TEX_{86}$. The reconstruction may, however, be biased to summer SSTs. The simulated monthly mean Arctic SSTs vary between 276 and 280 K. Thus the simulated Arctic surface is 11 to 13 K colder than inferred by Sluijs et al. (2006).

Note that annual mean sea surface temperatures in the proto Labrador Sea, which is close to the lower vertebrate findings of Estes and Hutchinson (1980), amount to about 290 K. According to Markwick (1998), the minimum thermal limit for crocodiles




is a coldest-month mean temperature of 278.7 K. While the coldest-month Labrador Sea surface temperature amounts to more than 285 K, the coldest-month land surface temperatures in the vicinity of the Labrador Sea fall just below 270 K. North American continental temperatures east of the Rocky Mountains amount to more than 285 K, and monthly means are above freezing all year round south of 55° N in that area. This relatively warm continental area matches the area where Markwick (1994) found most fossil crocodiles.

### 3.3 PE-PR temperature differences

The PE surface is on average 9.4 K warmer than the PR surface (Table 2). We find a large high-latitude amplification of this warming (Fig. 5b). The low-latitude zonal mean PE surface temperatures are about 5 to 8 K warmer than in PR, while northern high latitudes are warmer by up to 20 K, and southern high latitudes are warmer by up to 40 K. The SST PE-PR differences are smallest in the South Atlantic and North and South Pacific subtropical gyres at about ±15° N. The PE zonal mean SSTs are about 5 K warmer at low latitudes, about 10 K warmer in the Southern Ocean, and up to 12 K warmer at 45° N.

While the surface temperature PE-PR difference increases towards higher latitudes, the SST PE-PR difference north of 50° N decreases towards the North Pole. This difference occurs because the SSTs in PR cannot fall below the freezing point of sea water. Over land, the surface temperature as defined in ECHAM5 is computed from the energy balance at the land surface - atmosphere interface. It is not identical but close to the 2 m air temperature. Over water, the surface temperature in ECHAM5 is identical to the SST, which in MPI-OM is the mean temperature of the uppermost, 12 m thick level. In the presence of sea ice, the surface temperature is defined as the temperature at the sea ice-atmosphere interface. Note that PE is basically sea ice free (Sect. 3.1), while PR has sea ice both in the Northern and in the Southern Hemisphere. At least 80% of the PR Arctic ocean remain sea-ice covered all year round, the average sea ice thickness amounts to about 3 m. During the Northern Hemisphere winter, the sea

ice extends to about 50° N. The Antarctic sea ice border in the Southern Hemisphere winter reaches about 65° S, most of the Antarctic sea ice is less than 1 m thick.

### 3.4 Differences in the hydrological cycle

Compared to PR, the PE hydrological cycle is intensified by about 25% (Fig. 6). Convective precipitation is higher by about 0.3 m per year (20 to 30%) at low latitudes between ±10° N. Also, convective precipitation is higher by about 0.2 m per year at latitudes higher than 30°, which is remarkable since there is hardly any convective precipitation at high latitudes in PR. This is consistent with the hypothesis that convective clouds cause high-latitude warming in PE (Abbot and Tziperman, 2008). The PE peak large-scale precipitation is higher than in PR by more than 0.2 m per year, and it is shifted to higher latitudes. Snowfall is reduced and occurs at higher latitudes only. Evaporation is enhanced by −0.2 to −0.4 m per year with the largest absolute changes in the Northern Hemisphere low latitudes, and the largest relative changes at the poles.

### 3.5 Meridional heat transport

The total PE and PR atmospheric heat transports are fairly symmetric about the equator, with maximum poleward transports of about 5.3 PW (1 PW=$10^{15}$ W) at ±40° N. We find that the meridional transport of latent heat is increased in PE compared to PR, especially the poleward transports around ±45° N, and the equatorward transport in the northern Hadley cell (around 15° N). The meridional transports of dry static energy reduce such that the total atmospheric heat transport in PE and PR hardly differ from each other (Fig. 7a).

The maximum northward oceanic heat transport in PE is about 0.5 PW smaller than in PR. We find that most of this difference is due to a decreased heat transport by the meridional overturning circulation (MOC, see Fig. 7b). However, the poleward oceanic gyre heat transport across 45° N is also reduced by almost 0.4 PW in PE compared to PR.

## 4 Analysis of mechanisms causing PE-PR differences

The aim of this section is to isolate and quantify the most important mechanisms that lead to the surface temperature differences between PE and PR.

### 4.1 Zero-dimensional energy balance model (EBM)

The Earth's surface in PE is on average 9.4 K warmer than in PR (Table 2). To better understand this large difference in surface temperature, we first compare the planetary albedos and the effective longwave emissivities in PE to those in PR. The PE planetary albedo is smaller by 0.026 (Table 2); less shortwave radiation is reflected by the atmosphere. This causes PE to be warmer than PR. The PE effective longwave emissivity is smaller by 0.044; the fraction of the longwave radiation emitted at the surface and leaving the top of the atmosphere is reduced. This also causes PE to be warmer than PR.

To quantify these effects, we apply a zero-dimensional energy balance model (EBM) that equates incoming shortwave radiation and outgoing longwave radiation for a grey atmosphere:

$$\frac{S_0}{4}(1-\alpha) = \epsilon\sigma\tau_{s,\mathrm{ebm}}^4 \tag{1}$$

where $\tau_{s,\mathrm{ebm}}$ is the surface temperature predicted by the EBM, $S_0$=1367 $\mathrm{Wm}^{-2}$ the total solar irradiance, and $\sigma$=5.67·10$^{-8}$ $\mathrm{Wm}^{-2}\,\mathrm{K}^{-4}$ the Stefan-Boltzmann constant. The factor 1/4 accounts for the difference between the area of the circular Earth profile in the sunshine, and the area of the spherical Earth. We derive the planetary albedo $\alpha$ and the effective longwave emissivity $\epsilon$ from the globally averaged radiative fluxes in our coupled GCM

$$\alpha = \frac{SW_t^{up}}{SW_t^{\mathrm{down}}}, \quad \epsilon = \frac{LW_t^{up}}{LW_s^{up}} \tag{2}$$



CPD
5, 1297–1336, 2009



where $SW_t^{up}$ and $SW_t^{\text{down}}$ are the upward and downward shortwave fluxes at the top of the atmosphere, and $LW_t^{up}$ and $LW_s^{up}$ are the upward longwave fluxes at the top of the atmosphere and the surface, respectively.

The EBM (Eq. 1), fed with these albedos and emissivities, yields surface temperatures of 298.0 K and 289.5 K for the PE and PR simulations, respectively (Table 2). These temperatures are off the general circulation model (GCM) temperatures by less than 2 K. The EBM temperature difference of about 8.5 K compares relatively well to the 9.4 K temperature difference in the GCM. According to the EBM, about 5.7 K of the warming are due to the reduced emissivity of longwave radiation, and about 2.8 K are due to the reduced planetary albedo (Fig. 8).

The PE-PR *planetary* albedo difference is a consequence of the by 0.043 smaller PE *surface* albedo. The largest zonal mean PE-PR surface albedo differences are located at high latitudes (Fig. 9). This is in part caused by our assumption that there are no glaciers in PE. The other main factor is that PE, in contrast to PR, is basically sea ice free. Moreover, there is less high-latitude snowfall in PE compared to PR (Sect. 3.1). Notice that the planetary albedo change is smaller than the surface albedo change because of cloud effects (see Sect. 4.2).

### 4.2 Cloud radiative forcing

To estimate the effect of clouds in both GCM simulations, we again apply the EBM (Eq. 1). This time, however, we use the *clear sky* radiative fluxes to compute the clear sky albedo $\alpha_c$ and clear sky effective longwave emissivity $\epsilon_c$

$$\alpha_c = \frac{SW_{t,c}^{up}}{SW_t^{\text{down}}}, \quad \epsilon_c = \frac{LW_{t,c}^{up}}{LW_s^{up}} \tag{3}$$

where $SW_{t,c}^{up}$ is the upward clear sky shortwave flux, and $LW_{t,c}^{up}$ is the upward clear sky longwave flux at the top of the atmosphere. Note that the surface emits longwave radiation depending on the surface temperature, no matter what the cloudiness. The

clear sky fluxes in ECHAM5 are computed assuming that there are no clouds; the difference between the albedos/emissivities computed from the clear sky and full sky fluxes thus yields the effect of clouds.

We find that clouds cause a 1 K stronger cooling in PE than in PR (namely 6.5 K compared to 5.5 K, see Fig. 10). This is due to a larger increase of the planetary albedo in PE compared to PR. The planetary albedo increase due to clouds amounts to 0.159 for PE and only 0.145 for PR. By multiplication with $S_0/4$, this translates into a shortwave cloud radiative forcing (CRF) of $-54.3\,Wm^{-2}$ in PE compared to $-49.6\,Wm^{-2}$ in PR. Note that this larger negative shortwave CRF in PE occurs despite a reduced total cloud cover (Table 2). Even though the cloud cover is reduced, the shortwave effect of the clouds is larger in PE because the surface is darker. According to the EBM, the PE shortwave CRF causes a cooling of 15.0 or 15.5 K, depending on wether we change the albedo or the emissivity first (black auxiliary lines in Fig. 10 are only drawn for emissivity decrease first). The pre-industrial shortwave CRF causes a cooling of 13.9 or 14.3 K. The difference of 0.7 to 1.6 K is reduced by about 0.2 K due to a larger positive longwave CRF for PE ($29.6\,Wm^{-2}$ compared to $28.8\,Wm^{-2}$). This larger longwave CRF in PE occurs despite a smaller emissivity change, because the absolute amount of longwave radiation emitted from the surface is much larger ($445\,Wm^{-2}$ compared to $395\,Wm^{-2}$, Table 2).

Note that the global mean PE-PR emissivity difference due to cloud cover changes is small only because the reduced emissivity due to clouds at high latitudes is overcompensated by an increased low latitude emissivity (grey lines in Figs. 9b–c and 11). Thus, cloud changes via absorption of longwave radiation cause a high-latitude amplification of the PE-PR temperature difference. On the other hand, clouds via the reflection of shortwave radiation diminish the high-latitude amplification due to surface albedo changes (Figs. 9a and 11).





### 4.3 Topographic changes

Some of the regional PE-PR surface temperature differences are caused by topographic height changes. To estimate this effect, we compare the PE-PR surface temperature difference to the potential temperature difference. We compute the potential temperatures at the global mean surface pressure, assuming a dry adiabatic lapse rate of $9.8\,\mathrm{K(km)}^{-1}$. We find the largest topographic effects in Antarctica, where the lower PE orography accounts for a zonal mean surface warming of up to 15 K, and in the present day Himalaya, where it accounts for a surface warming of about 3 K (compare solid black to grey line in Fig. 5b). The global mean spectrally averaged surface height in PE is about 90 m lower than in PR (Table 2). The global mean PE and PR potential temperatures at the respective mean sea level pressures differ by 0.9 K less than the global mean surface temperatures. However, since the global mean surface pressure in ECHAM5 is prescribed at 985.5 hPa (the atmosphere does not change its mass), the variation of the global mean surface height does not influence the global mean surface temperature.

### 4.4 Greenhouse gas forcing

As we have seen in Sect. 4.2, clouds only slightly affect the global mean PE-PR emissivity difference. The non-$CO_2$ well-mixed greenhouse gases in the PE simulation are kept at pre-industrial levels (Table 1). Hence the lower emissivity in the PE simulation should be due to the doubled $CO_2$ concentration and an increased atmospheric water vapour content. A doubled $CO_2$ concentration yields an additional radiative forcing of $3.7\,\mathrm{Wm}^{-2}$ (e.g., Forster et al., 2007). The temperature change due to this additional radiative forcing can be computed from

$$\frac{S_0}{4}(1-\alpha) + 3.7\,\mathrm{Wm}^{-2} \equiv \epsilon\sigma\tau'^4_{s,\mathrm{ebm}} \tag{4}$$

which defines the changed surface temperature $\tau'_{s,\mathrm{ebm}}$, and results in

$$\tau'_{s,\mathrm{ebm}} - \tau_{s,\mathrm{ebm}} \approx 1.1\,\mathrm{K}. \tag{5}$$

The globally averaged, vertically integrated atmospheric water vapour content has almost doubled in PE compared to PR (Table 2). Note the large relative changes of the water vapour content at high latitudes (Fig. 12). Unfortunately, we cannot diagnose the radiative forcing of this water vapour increase directly from our GCM setup; however, we can compute the water vapour effect as a residual. The total PE-PR surface temperature difference due to emissivity changes amounts to +5.7 K (Sect. 4.1). The stronger positive longwave CRF in PE only yields about +0.2 K (Sect. 4.2). Doubled $pCO_2$ yields +1.1 K. The residual, which we ascribe to the larger PE atmospheric water vapour content, amounts to +4.4 K.

### 4.5 Orbital forcing

The choice of the orbital parameters as described in Sect. 2 leads to the following changes in PE, compared to PR: less incoming shortwave radiation in the Northern Hemisphere in May, June, and July; less incoming radiation in the Arctic spring and autumn; and more radiation mostly during December and January in low and mid latitudes (Fig. 13a). Integrated over the annual cycle, this amounts to about 0.3 $Wm^{-2}$ more incoming shortwave radiation at low and middle latitudes in PE, and about 1 $Wm^{-2}$ less incoming shortwave radiation at high latitudes (Fig. 13b). This redistribution of the incoming shortwave radiation at the top of the atmosphere, from high latitudes to low latitudes, is due to the reduced obliquity in PE (Fig. 2).

As mentioned in Sect. 2, the orbital parameters obliquity, eccentricity, and longitude of perihelion vary on timescales that are short compared to the length of the PE period. Changes of these parameters do not lead to a change of the global mean incoming shortwave radiation and thus should not, in the first approximation, affect the global mean temperature. However, other results might change; for example, choosing a larger obliquity in our PE setup would have caused a smaller pole-to-equator temperature gradient.

From the theory of stellar evolution, it is known that the Sun has gradually brightened by more than 30% since it settled down to steady nuclear burning of hydrogen roughly

4.5 billion years ago (e.g., Endal and Sofia, 1981; Peltier, 2003). Due to this brightening, the total solar irradiance 55 Ma ago was up to 0.6% (about 8 $Wm^{-2}$) smaller than at present. According to the EBM (Eq. 1), and given the PE albedos and emissivities, the temperature change due to such a reduction of the radiative forcing would amount to less than −0.5 K.

## 5 Discussion and conclusions

Using the coupled atmosphere-ocean-sea ice general circulation model ECHAM5/MPI-OM, we perform a long, stable climate simulation for the late Paleocene/early Eocene (PE). The simulated PE Earth surface is on average 297 K warm and ice-free. To our knowledge, we have obtained the first coupled PE simulation with moderate GHG forcing that is warm enough at high latitudes to keep the poles free from sea ice, while reasonably matching the lower latitude SST reconstructions. However, if we take the SST proxy data by Sluijs et al. (2006) at face value, the simulated Arctic surface temperature is still too cold.

A possible shortcoming of this study is the assumption of a globally homogeneous vegetation. Including a more realistic vegetation distribution such as the one reconstructed by Utescher and Mosbrugger (2007) may, at least regionally, affect the climate (Sewall et al., 2000). Also, we did not include lakes in our PE model setup. Including lakes (e.g., the North American Green River lake system) could lead to a further reduction of the seasonality in the continental interiors (Sloan, 1994).

We find that the *total* atmospheric heat transports in PE and the pre-industrial reference (PR) are very similar, although the latent heat fraction is larger in PE than in PR. The total poleward heat transport by the ocean is smaller in PE compared to PR. We conclude that meridional heat transports do not contribute to the more equable PE climate in our simulation (confirming the results of Huber and Sloan, 2001). A more detailed analysis of the PE ocean circulation will be subject of a future study.

Compared to PR, the simulated PE Earth surface is on average 9.4 K warmer. While low latitudes in PE compared to PR are on average about 5 to 8 K warmer, northern

high latitudes are warmer by up to 20 K, and southern high latitudes are warmer by up to 40 K. As a diagnostic tool to roughly understand this temperature difference, we fit a zero-dimensional energy balance model (EBM) to the PE and PR GCM solutions.

According to the EBM, one third of the PE-PR surface temperature difference is due to a reduced planetary albedo. The surface albedo in PE compared to PR is reduced mostly due to the lack of glaciers, the lack of sea ice, and reduced snowfall. However, this large high-latitude surface albedo change is partly compensated by a more negative shortwave cloud radiative forcing. In that sense, clouds in our PE model work against the high-latitude amplification of the snow and ice albedo feedback. Nevertheless, the planetary albedo reduction is largest at high latitudes.

Two thirds of the warming are due to a reduction of the effective longwave emissivity. We find that clouds cause a significant reduction of the effective longwave emissivity at high latitudes. This reduction of the emissivity at high latitudes is overcompensated by an increase of the emissivity due to clouds at lower latitudes. This way (via their effect on the longwave emissivity), clouds in PE compared to PR hardly affect the global mean temperature, but they cause a polar warming and a tropical cooling.

The doubled atmospheric $pCO_2$ directly causes a warming of about 1 K. We ascribe the residual of the emissivity-induced PE-PR temperature difference, which amounts to more than 4 K, to the water vapour feedback. The emissivity change due to the combination of the doubled $pCO_2$ and the water vapour feedback is also largest at high latitudes, and thus leads to a high-latitude amplification.

The reduced orographic height in the PE setup should not affect the global mean temperature, but it does have large regional effects. Up to 15 K of the southern high-latitude PE-PR surface temperature difference is due to the lower Antarctic surface height in PE.

As a consequence of the reduced obliquity in our PE setup, a small amount of incoming shortwave radiation at the top of the atmosphere is redistributed from high latitudes to low latitudes. The resulting annual mean reduction of the radiative forcing by about 1 $Wm^{-2}$ at high latitudes should only slightly increase the pole-to-equator temperature

gradient in the PE simulation. Note that, for comparison, the cloud-induced emissivity reduction at high latitudes yields an additional, annual mean CRF of up to 20 $Wm^{-2}$.

Summing up, the equable PE climate as simulated in ECHAM5/MPI-OM is due to topographic effects, due to surface albedo changes, and most importantly due to a reduction of the effective longwave emissivity that is largest at high latitudes.

*Acknowledgements.* We thank Helmuth Haak for his help setting up the PE model, and for providing the pre-industrial reference simulation. We thank Karen Bice for advice, and for providing the paleo-topography. The model experiments were carried out on the supercomputing system of the German Climate Computation Centre (DKRZ) Hamburg. This work was completed during a Gary C. Comer Science and Education Foundation Abrupt Climate Change Fellowship.

The service charges for this open access publication have been covered by the Max Planck Society.

## References

Abbot, D. S. and Tziperman, E.: Sea ice, high-latitude convection, and equable climates, Geophys. Res. Lett., 35, 1–5, 2008. 1300, 1309

Alley, R. B., Marotzke, J., Nordhaus, W., Overpeck, J., Peteet, D., Jr., R. P., Pierrehumbert, R., Rhines, P., Stocker, T., Talley, L., and Wallace, J. M.: Abrupt Climate Change: Inevitable Surprises, National Academy Press, 2002. 1300

Arakawa, A. and Lamb, V. R.: Computational design of the basic dynamical processes of the CLA general circulation model, Methods Comput. Phys., 17, 173–265, 1977. 1303

Barron, E. J.: Eocene equator-to-pole surface ocean temperatures: a significant climate problem?, Paleoceanography, 2, 729–739, 1987. 1299

Berger, A. L.: Long Term Variations of Daily Insolation and Quaternary Climatic Changes, J. Atmos. Sci., 35, 2362–2367, 1978. 1322, 1325

Bice, K. L. and Marotzke, J.: Numerical evidence against reversed thermohaline circulation in the warm Paleocene/Eocene ocean, J. Geophys. Res., 106, 11529–11542, 2001. 1302, 1304





Bice, K. L. and Marotzke, J.: Could changing ocean circulation have destabilized methane hydrate at the Paleocene/Eocene boundary?, Paleoceanography, 17, doi:10.1029/2001PA000678, 2002. 1304
Bretagnon, P. and Francou, G.: Planetary theories in rectangular and spherical variables – VSOP 87 solutions, Astron. Astrophys., 202, 309–315, 1988. 1305, 1322
Covey, C. and Barron, E.: The Role of Ocean Heat Transport in Climatic Change, Earth-Sci. Rev., 24, 429–445, 1988. 1299
Dickens, G. R., O'Neil, J. R., Rea, D. K., and Owen, R. M.: Dissociation of oceanic methane hydrate as a cause of the carbon isotope excursion at the end of the Paleocene, Paleoceanography, 10, 965–971, 1995. 1300
Endal, A. S. and Sofia, S.: Rotation of Solar Type Stars. I. Evolutionary Models for the Spindown of the Sun, Astrophys. J., 243, 625–640, 1981. 1315
Estes, R. and Hutchinson, J. H.: Eocene lower vertebrates from Ellesmere Island, Canadian Arctic Archipelago, Palaeogeogr. Palaeocl., 30, 325–347, 1980. 1299, 1307
Forster, P., Ramaswamy, V., Artaxo, P., Berntsen, T., Betts, R., Fahey, D., Haywood, J., Lean, J., Lowe, D., Myhre, G., Nganga, J., Prinn, R., Raga, G., Schulz, M., and Dorland, R. V.: Changes in Atmospheric Constituents and in Radiative Forcing, in: Climate Change 2007: The Physical Science Basis. Contribution of Working Group I to the Fourth Assessment Report of the Intergovernmental Panel on Climate Change, edited by: Solomon, S., Qin, D., Manning, M., Chen, Z., Marquis, M., Averyt, K. B., Tignor, M., and Miller, H. L., 129–234, Cambridge University Press, Cambridge, United Kingdom and New York, NY, USA, 2007. 1313
Fortuin, J. P. F. and Kelder, H.: An ozone climatology based on ozonesonde and satellite measurements, J. Geophys. Res.-Atmos., 103, 31709–31734, 1998. 1302
Fouquart, Y. and Bonnel, B.: Computations of solar heating of the earth's atmosphere: A new parameterization, Beitr. Phys. Atmos., 53, 35–62, 1980. 1302
Gent, P. R., Willebrand, J., McDougall, T., and McWilliams, J. C.: Parameterizing eddy-induced tracer transports in ocean circulation models, J. Phys. Oceanogr., 25, 463–474, 1995. 1304
Greenwood, D. R. and Scott, L. W.: Eocene continental climates and latitudinal temperature gradients, Geology, 23, 1044–1048, 1995. 1299
Griffies, S. M.: The Gent-McWilliams skew flux, J. Phys. Oceanogr., 28, 831–841, 1998. 1304
Hagemann, S.: Report No. 336: An Improved Land Surface Parameter Dataset for Global and Regional Climate Models, Tech. rep., Max Planck Institute for Meteorology, Hamburg,




Germany, 2002. 1303
Hagemann, S., Botzet, M., Dümenil, L., and Machenhauer, B.: Report No. 289: Derivation of global GCM boundary conditions from 1 km land use satellite data, Tech. rep., Max Planck Institute for Meteorology, Hamburg, Germany, 1999. 1303
Hibler, W. D.: A Dynamic Thermodynamic Sea Ice Model, J. Phys. Oceanogr., 9, 815–846, 1979. 1304
Huber, M.: Climate Change: A Hotter Greenhouse?, Science, 321, 353–354, 2008. 1299
Huber, M. and Sloan, L. C.: Heat transport, deep waters, and thermal gradients: Coupled simulation of an Eocene Greenhouse Climate, Geophys. Res. Lett., 28, 3481–3484, 2001. 1299, 1315
Huber, M., Sloan, L. C., and Shellito, C.: Early Paleogene oceans and climate: a fully coupled modelling approach using NCAR's CCSM, in: Causes and Consequences of Globally Warm Climates in the Early Paleogene, edited by: Wing, S. L., Gingerich, P. D., Schmitz, B., Thomas, E., Geological Society of America Special Paper, 369, 25–47, 2003. 1306
Jungclaus, J. H., Keenlyside, N., Botzet, M., Haak, H., Luo, J.-J., Latif, M., Marotzke, J., Mikolajewicz, U., and Roeckner, E.: Ocean Circulation and Tropical Variability in the Coupled Model ECHAM5/MPI-OM, J. Climate, 19, 3952–3972, 2006. 1304, 1305
Kump, L. R. and Pollard, D.: Amplification of Cretaceous Warmth by Biological Cloud Feedbacks, Science, 320, 195, 2008. 1300
Laskar, J., Robutel, P., Joutel, F., Gastineau, M., Correia, A. C. M., and Levrard, B.: A long term numerical solution for the insolation quantities of the Earth, Astron. Astrophys., 428, 261–285, 2004. 1303, 1325
Lin, S. J. and Rood, R. B.: Multidimensional flux-form semi-Lagrangian transport, Mon. Weather Rev., 124, 2046–2068, 1996. 1302
Lohmann, U. and Roeckner, E.: Design and performance of a new cloud microphysics parameterization developed for the ECHAM4 general circulation model, Clim. Dynam., 12, 557–572, 1996. 1302
Lott, F. and Miller, M. J.: A new subgrid-scale orographic drag parameterization: 1st formulation and testing, Q. J. Roy. Meteor. Soc., 123, 101–127, 1997. 1302
Luo, J.-J., Massen, S., Roeckner, E., Madec, G., and Yamagata, T.: Reducing climatology bias in an ocean-atmosphere CGCM with improved coupling physics, J. Climate, 18, 2344–2360, 2005. 1304
Markwick, P. J.: "Equability," continentality, and Tertiary "climate": The crocodilian perspective,




Geology, 22, 613–616, 1994. 1299, 1308
Markwick, P. J.: Fossil crocodilians as indicators of Late Cretaceous and Cenozoic climates: implications for using palaeontological data in reconstructing palaeoclimate, Palaeogeogr. Palaeocl., 137, 205–271, 1998. 1299, 1307
Marsland, S. J., Haak, H., Jungclaus, J. H., Latif, M., and Röske, F.: The Max-Planck-Institute global ocean/sea ice model with orthogonal curvilinear coordinates, Ocean Modell., 5, 91–127, 2003. 1303, 1304, 1305
Mlawer, E. J., Taubman, S. J., Brown, P. D., Iacono, M. J., and Clough, S. A.: Radiative transfer for inhomogeneous atmospheres: RRTM, a validated k-correlated model for the longwave, J. Geophys. Res., 102, 16663–16682, 1997. 1302
Pacanowski, R. C. and Philander, S. G. H.: Parameterization of vertical mixing in numerical models of tropical oceans, J. Phys. Oceanogr., 11, 1443–1451, 1981. 1304
Pearson, P. N. and Palmer, M. R.: Atmospheric carbon dioxide concentrations over the past 60 million years, Nature, 406, 695–699, 2000. 1302
Peltier, W. R.: Earth System History, in: Encyclopedia of Global Environmental Change, Volume One, The Earth system: physical and chemical dimensions of global environmental change, 31–60, John Wiley & Sons, Ltd, 2003. 1315
Roeckner, E., Bäuml, G., Bonaventura, L., Brokopf, R., Esch, M., Giorgetta, M., Hagemann, S., Kirchner, I., Kornblueh, L., Manzini, E., Rhodin, A., Schlese, U., Schulzweida, U., and Tompkinsi, A.: The atmospheric general circulation model ECHAM5, Tech. rep., Max Planck Institute for Meteorology, Hamburg, Germany, available online at http://www.mpimet.mpg.de, 2003. 1301
Royer, D. L., Wing, S. L., Beerling, D. J., Jolley, D. W., Koch, P. L., Hickey, L. J., and Berner, R. A.: Paleobotanical evidence for near present-day levels of atmospheric $CO_2$ during part of the tertiary, Science, 292, 2310–2313, June, 2001. 1302
Semtner, A. J.: A Model for the Thermodynamic Growth of Sea Ice in Numerical Investigations of Climate, J. Phys. Oceanogr., 379–389, 1976. 1304
Sewall, J. O., Sloan, L. C., Huber, M., and Wing, S.: Climate sensitivity to changes in land surface characteristics, Global Planet. Change, 26, 445–465, 2000. 1315
Sexton, A. J., Wilson, P. A., and Pearson, P. N.: Microstructural and geochemical perspectives on planktic foraminiferal preservation: “Glassy” versus “Frosty”, Geochem. Geophy. Geosy., 7, 2006. 1299
Shackleton, N. and Boersma, A.: The climate of the Eocene ocean, J. Geol. Soc. London, 138,

153–157, 1981. 1299
Shellito, C. J., Sloan, L. C., and Huber, M.: Climate model sensitivity to atmospheric $CO_2$ levels in the Early-Middle Paleogene, Palaeogeogr. Palaeocl., 193, 113–123, 2003. 1299
Sloan, L. C.: Equable climates during the early Eocene: significance of regional paleogeography for North American climate, Geology, 22, 881–884, 1994. 1315
Sloan, L. C. and Pollard, D.: Polar stratospheric clouds: A high latitude warming mechanism in an ancient greenhouse world, Geophys. Res. Lett., 25, 3517–3520, 1998. 1300
Sloan, L. C., Walker, J. C. G., and Moore Jr., T. C.: Possible role of oceanic heat transport in early Eocene climate, Paleoceanography, 10, 347–356, 1995. 1299
Sluijs, A., Schouten, S., Pagani, M., Woltering, M., Brinkhuis, H., Damste, J. S. S., Dickens, G. R., Huber, M., Reichart, G.-J., Stein, R., Matthiessen, J., Lourens, L. J., Pedentchouk, N., Backman, J., Moran, K., and the Expedition 302 Scientists: Subtropical Arctic Ocean temperatures during the Palaeocene/Eocene thermal maximum, Nature, 441, 610–613, 2006. 1299, 1307, 1315, 1328
Tanré, D., Geleyn, J.-F., and Slingo, J. M.: First results of the introduction of an advanced aerosol-radiation interaction in the ECMWF low resolution global model, in: Aerosols and their climatic effects, 133–177, 1984. 1302
Thomas, D. J., Zachos, J. C., Bralower, T. J., Thomas, E., and Bohaty, S.: Warming the fuel for the fire; evidence for the thermal dissociation of methane hydrate during the Paleocene-Eocene thermal maximum, Geology, 30, 1067–1070, 2002. 1299, 1328
Tripati, A. and Elderfield, H.: Abrupt hydrographic changes in the equatorial Pacific and subtropical Atlantic from foraminiferal Mg/Ca indicate greenhouse origin for the thermal maximum at the Paleocene-Eocene Boundary, Geochem. Geophy. Geosy., 5, 2004. 1299, 1328
Utescher, T. and Mosbrugger, V.: Eocene vegetation patterns reconstructed from plant diversity – A global perspective, Palaeogeogr. Palaeocl., 247, 243–271, 2007. 1303, 1315
Zachos, J. C., Wara, M. W., Bohaty, S., Delaney, M. L., Petrizzo, M. R., Brill, A., Bralower, T. J., and Premoli-Silva, I.: A Transient Rise in Tropical Sea Surface Temperature During the Paleocene-Eocene Thermal Maximum, Science, 302, 1551–1554, 2003. 1299, 1328
Zachos, J. C., Schouten, S., Bohaty, S., Quattlebaum, T., Sluijs, A., Brinkhuis, H., Gibbs, S. J., and Bralower, T. J.: Extreme warming of mid-latitude coastal ocean during the Paleocene-Eocene Thermal Maximum: Inferences from $TEX_{86}$ and isotope data, Geology, 34, 737–740, 2006. 1299, 1328

**Table 1.** ECHAM5 input parameters as used in the PE model setup compared to those in the pre-industrial reference run (PR); FAO determines volumetric heat capacity and thermal diffusivity of soil; note that, while the PE land surface is homogeneous, the land surface parameters for PR are spatially variable; the PR values given here are mean values. The pre-industrial orbital parameters are given for the year 2000 AD according to Berger (1978) while, actually, the orbital parameters in PR vary temporally according to VSOP87 (Variations Séculaire des Orbites Planétaires, Bretagnon and Francou, 1988).

| *parameter* | *PE* | *PR* |
|---|---|---|
| carbon dioxide concentration ($pCO_2$) | 560 ppm | 278 ppm |
| methane concentration ($pCH_4$) | 0.8 ppm | 0.65 ppm |
| nitrous oxide concentration ($pN_2O$) | 0.288 ppm | 0.27 ppm |
| total solar irradiance ($S_0$) | 1367 W m$^{-2}$ | 1367 W m$^{-2}$ |
| eccentricity of the Earth's orbit | 0.0300 | 0.0167 |
| obliquity or inclination of the Earth's axis | 23.25° | 23.44° |
| longitude of perihelion | 270° | 283° |
| land surface background albedo | 0.16 | 0.25 |
| sea surface albedo | 0.07 | 0.07 |
| vegetation ratio | 0.6 | 0.4 |
| leaf area index (LAI) | 2.3 | 2.2 |
| forest fraction | 0.40 | 0.26 |
| maximum field capacity of soil (single bucket water height) | 1.2 m | 0.6 m |
| FAO soil data flag (1∼sand, 3∼mud, 5∼clay) | 3 | 2.6 |
| surface roughness length over land | 1.6 m | 1.6 m |



CPD
5, 1297–1336, 2009



**Table 2.** Some key global mean climate parameters; while $\tau_s$ is the global mean surface temperature as diagnosed from the GCM, $\tau_{s,\mathrm{ebm}}$ is the EBM derived surface temperature (see Eq. 1) using the GCM diagnosed planetary albedo $\alpha$ and effective longwave emissivity $\epsilon$, $\tau_{s,\mathrm{ebm},c}$ is computed from the clear sky values $\alpha_c$ and $\epsilon_c$.

| *parameter* | *PE* | *PR* |
|---|---|---|
| surface temperature $\tau_s$ | 297.0 K | 287.6 K |
| mean surface pressure | 985.5 hPa | 985.5 hPa |
| mean sea level pressure (SLP) | 1001 hPa | 1012 hPa |
| potential temperature at SLP | 298.4 K | 289.9 K |
| planetary albedo $\alpha$ | 0.292 | 0.318 |
| clear sky planetary albedo $\alpha_c$ | 0.133 | 0.173 |
| surface albedo $\alpha_s$ | 0.094 | 0.137 |
| effective emissivity $\epsilon$ | 0.541 | 0.585 |
| clear sky effective emissivity $\epsilon_c$ | 0.608 | 0.658 |
| surface temperature $\tau_{s,\mathrm{ebm}}$ | 298.0 | 289.5 |
| surface temperature $\tau_{s,\mathrm{ebm},c}$ | 304.9 | 295.7 |
| longwave cloud radiative forcing (CRF) | 29.6 $\mathrm{Wm}^{-2}$ | 28.8 $\mathrm{Wm}^{-2}$ |
| upward longwave radiation at the surface $LW_s^{up}$ | −445 $\mathrm{Wm}^{-2}$ | −395 $\mathrm{Wm}^{-2}$ |
| shortwave CRF | −54.3 $\mathrm{Wm}^{-2}$ | −49.6 $\mathrm{Wm}^{-2}$ |
| total cloud cover | 0.576 | 0.617 |
| vertically integrated water vapour | 45.3 $\mathrm{kg\,m}^{-2}$ | 25.5 $\mathrm{kg\,m}^{-2}$ |
| spectrally filtered surface height h | 141 m | 231 m |



CPD
5, 1297–1336, 2009



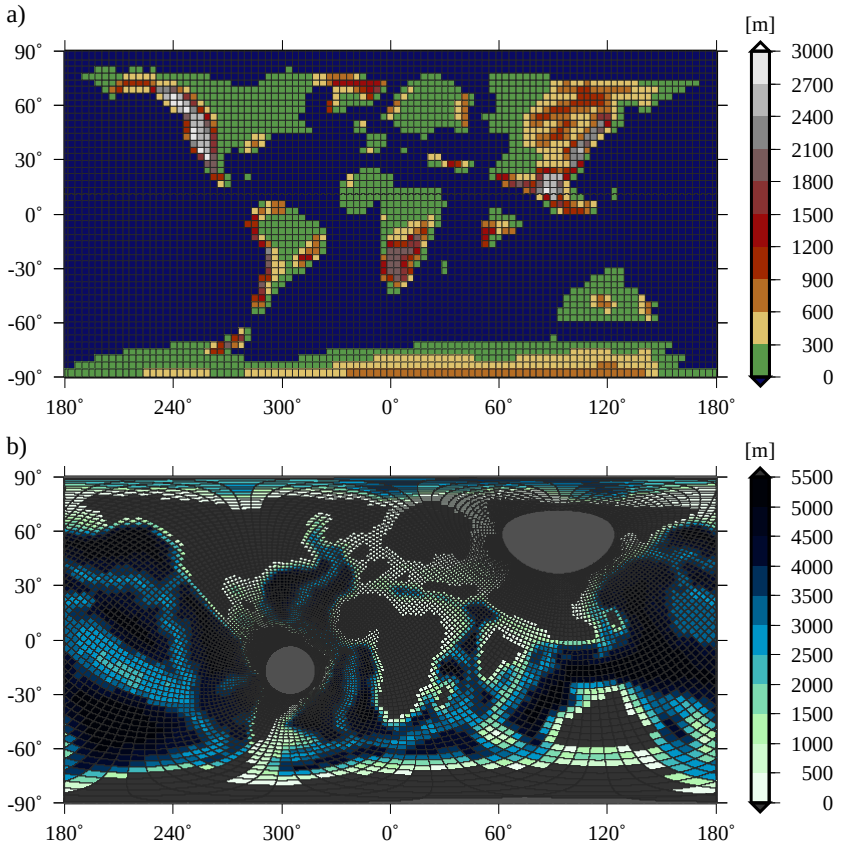


**Fig. 1. (a)** PE orography interpolated on the Gaussian grid that corresponds to the T31 spectral truncation; displayed orography not spectrally filtered. **(b)** PE bathymetry as used in MPI-OM.



CPD
5, 1297–1336, 2009



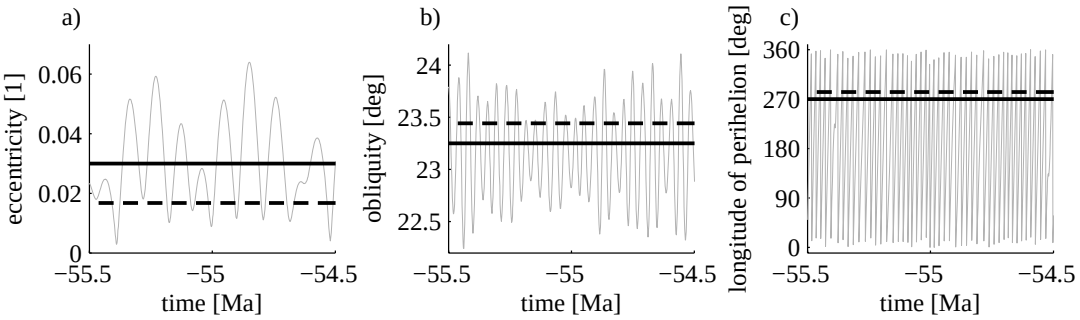


**Fig. 2.** **(a)** Eccentricity, **(b)** obliquity, and **(c)** longitude of perihelion as computed by Laskar et al. (2004) (thin grey line), constant values as used for the PE setup (heavy black), and pre-industrial values (heavy black, dashed; for the year 2000 AD according to Berger, 1978, see also Table 1).



CPD
5, 1297–1336, 2009



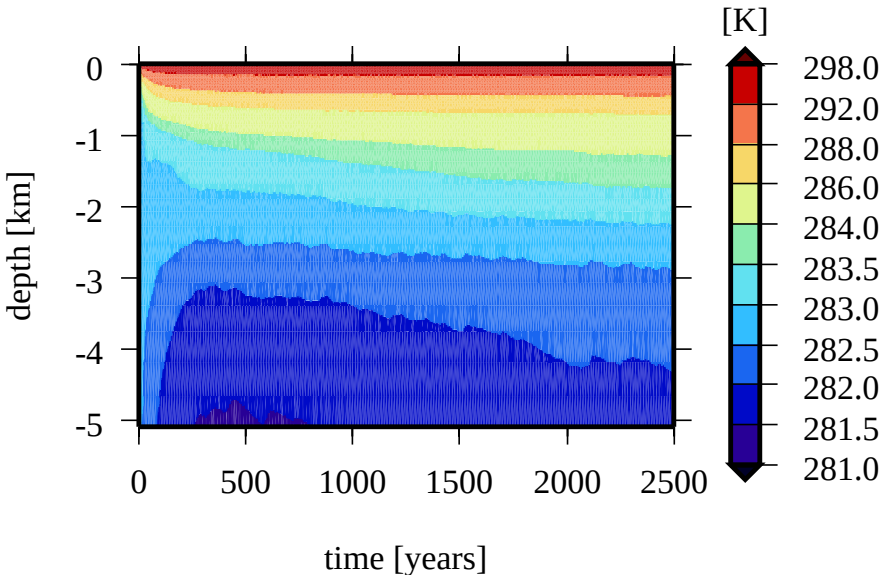


**Fig. 3.** Hovmöller diagram of the global ocean potential temperature in the PE simulation (50 year running mean).

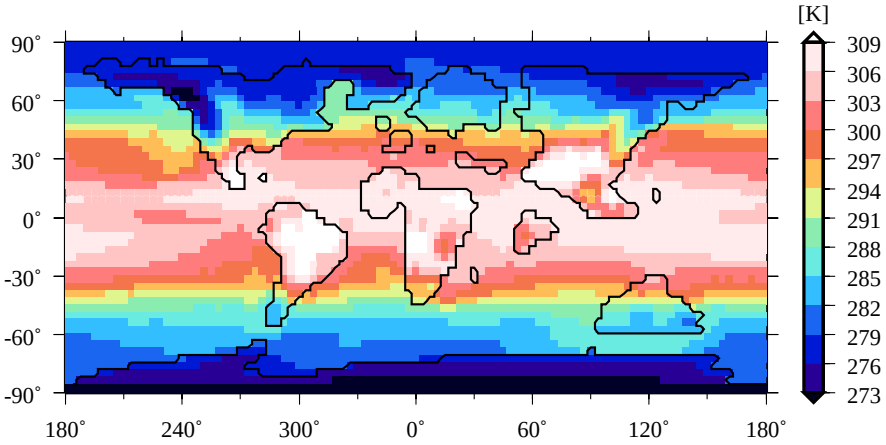


**Fig. 4.** Annual mean PE surface temperature (200 year mean).



CPD
5, 1297–1336, 2009



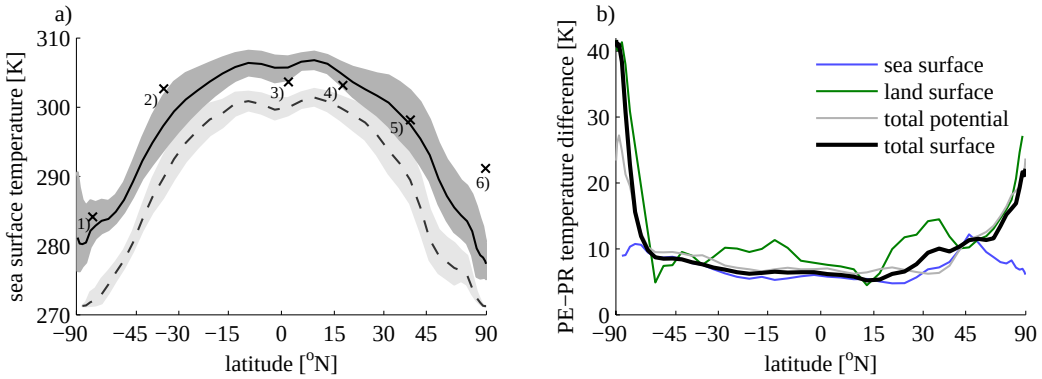


**Fig. 5. (a)** Sea surface temperature in PE (solid), and in PR (dashed); the shading indicates the seasonal variability of the 200-year climatology (differences between the warmest and coldest months); crosses are SST estimates from proxy data for the pre-PETM published by 1) Thomas et al. (2002) based on $\delta^{18}O$, 2) and 3) Tripati and Elderfield (2004) based on Mg/Ca ratios assuming the Mg/Ca ratio of seawater to be 5.15 mmol/mol, 4) Zachos et al. (2003) based on $TEX_{86}$, 5) Zachos et al. (2006) based on $TEX_{86}$, 6) Sluijs et al. (2006) based on $TEX_{86}$. **(b)** Annual mean temperature differences between PE and PR for the total surface (heavy, black), the dry potential temperature at the global mean surface pressure of 985.5 hPa (grey), only land surface (green), and only sea surface (blue). The horizontal scale is such that the spacing between the latitudes is proportional to the area of the Earth's surface between them, i.e., is linear in the sine of the latitude.



CPD
5, 1297–1336, 2009



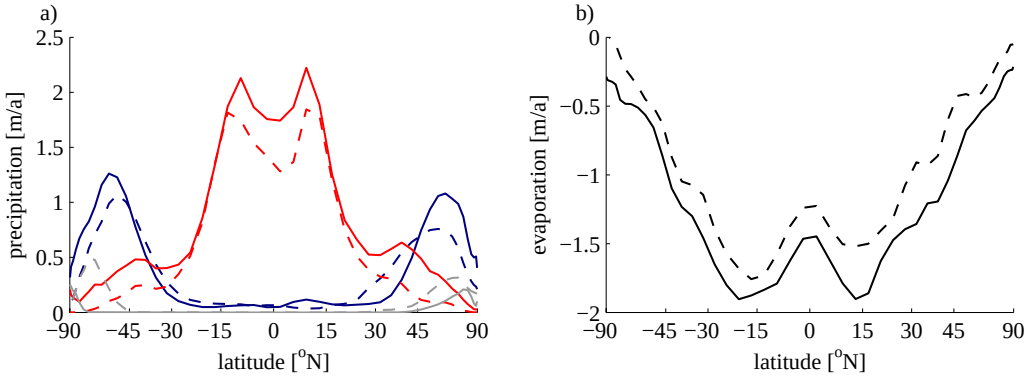


**Fig. 6. (a)** Zonal mean convective precipitation (red), large scale precipitation (dark blue), and snowfall (grey); **(b)** zonal mean evaporation; both precipitation and evaporation are diagnosed from the last 200 years of PE (solid) and PR (dashed). The horizontal scale is linear in the sine of the latitude.



CPD
5, 1297–1336, 2009



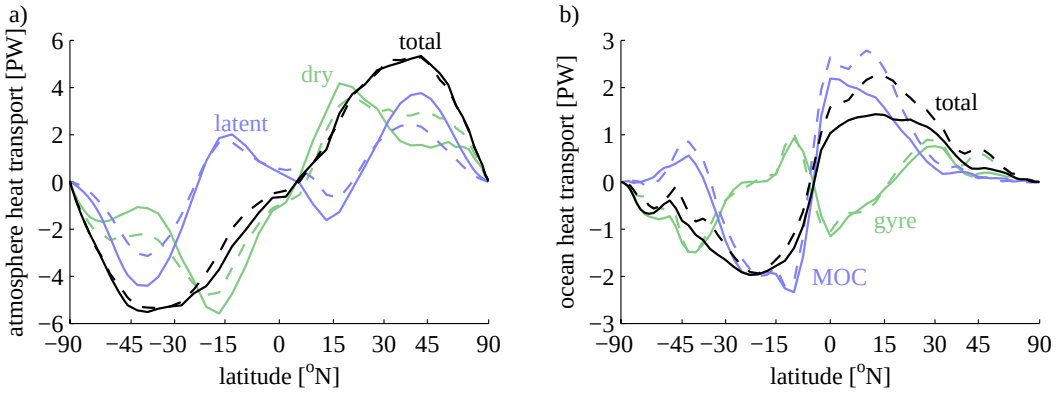


**Fig. 7. (a)** Zonally integrated meridional heat transport in the atmosphere due to the advection of dry air (green), due to the advection of moisture/latent heat (blue), and the sum (black), for PE (solid) and PR (dashed), computed from the last 100 years of each run with 6 hourly instantaneous sampling; **(b)** zonally integrated meridional ocean heat transport due to the meridional overturning circulation (MOC, blue), due to the gyre circulation (green), and the sum (black), for PE (solid) and PR (dashed), computed from monthly means of the last 1000 years of each run. The horizontal scale is linear in the sine of the latitude.



CPD
5, 1297–1336, 2009



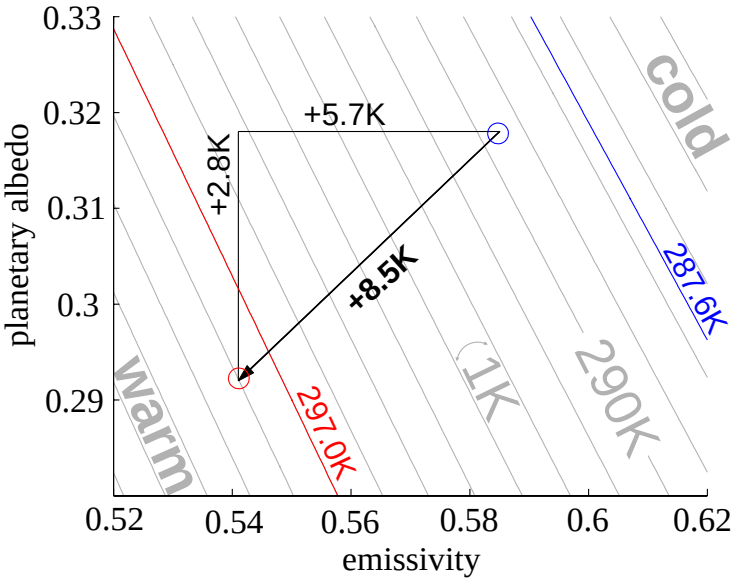


**Fig. 8.** Using the EBM to trace back the temperature difference between PE and PR to albedo and emissivity changes in the GCM; grey lines are contour lines of the EBM-predicted temperature for certain emissivities and albedos, contour intervals are 1 K; the red and blue lines are the GCM-diagnosed temperatures for PE and PR, respectively; the circles are the surface temperatures predicted by the EBM using the GCM-diagnosed emissivities and albedos; the black arrow indicates the EBM-predicted PE-PR temperature difference; the black lines are auxiliary lines to estimate the albedo and emissivity caused temperature difference separately.

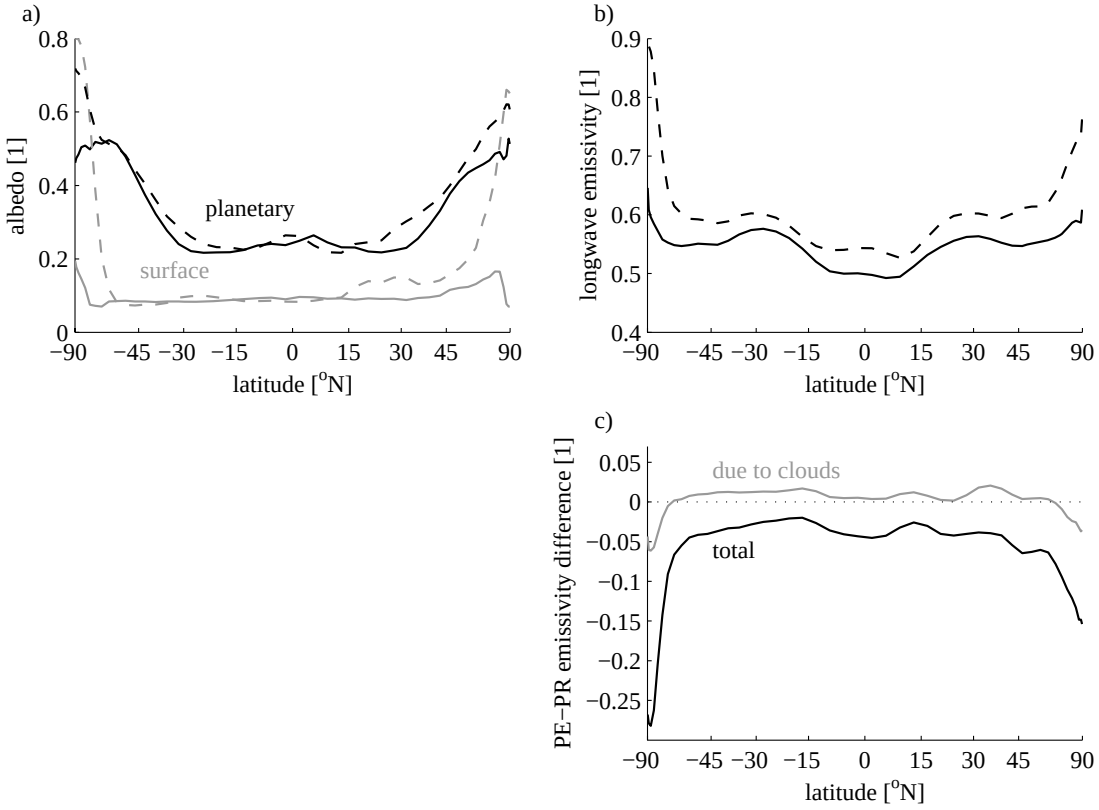


**Fig. 9.** **(a)** Zonal mean planetary (black) and surface (grey) albedo, **(b)** effective longwave emissivity for PE (solid) and PR (dashed), and **(c)** PE-PR emissivity change (black) and PE-PR emissivity change due to clouds (grey) diagnosed from the difference between the full sky and clear sky emissivities. The horizontal scale is linear in the sine of the latitude.



CPD
5, 1297–1336, 2009



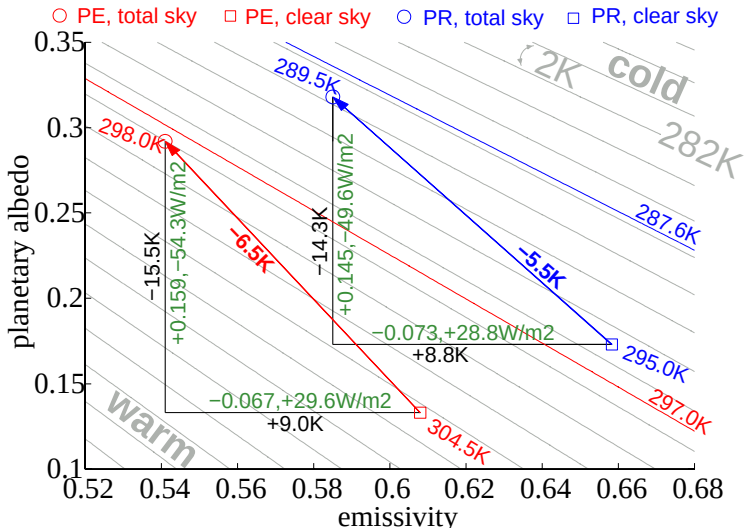


**Fig. 10.** Using the EBM to estimate the effect of clouds on the PE-PR temperature difference; grey lines are contour lines of the EBM-predicted temperature, contour intervals are 2 K; the red and blue lines are the GCM-diagnosed temperatures for PE and PR, respectively; the circles are the temperatures as computed from the EBM using the GCM-diagnosed *full sky* emissivities and albedos; the squares are EBM temperatures computed for the GCM-diagnosed *clear sky* emissivities and albedos; the red and blue arrows indicate the cooling due to clouds in PE and PR, respectively; the black lines are auxiliary lines to decompose the temperature differences into differences caused by albedo and emissivity; green numbers are emissivity and albedo changes due to clouds and the according cloud radiative forcing.



CPD
5, 1297–1336, 2009



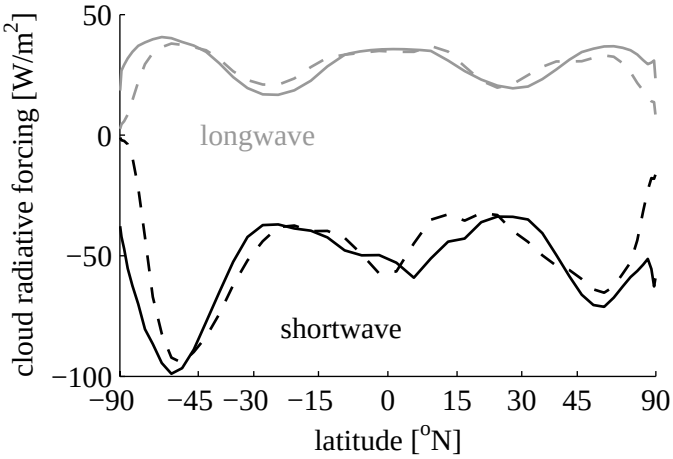


**Fig. 11.** Zonal mean longwave (grey) and shortwave (black) cloud radiative forcing as diagnosed from PE (solid), and PR (dashed). The horizontal scale is linear in the sine of the latitude.

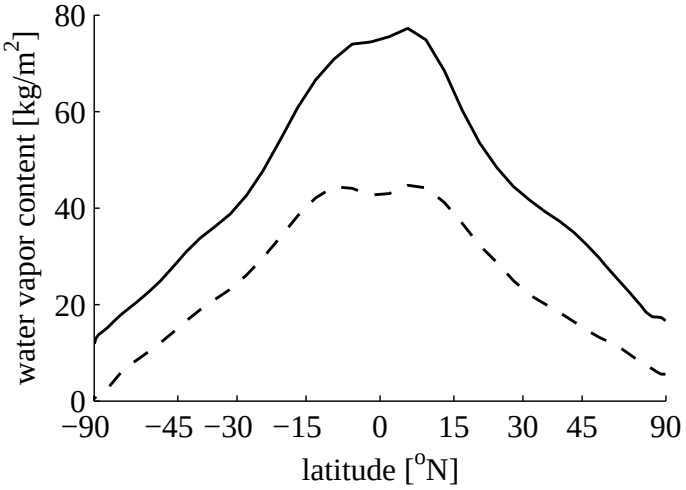


**Fig. 12.** Zonal mean vertically integrated water vapour in the PE simulation (solid) compared to the pre-industrial simulation (dashed). The horizontal scale is linear in the sine of the latitude.



CPD
5, 1297–1336, 2009



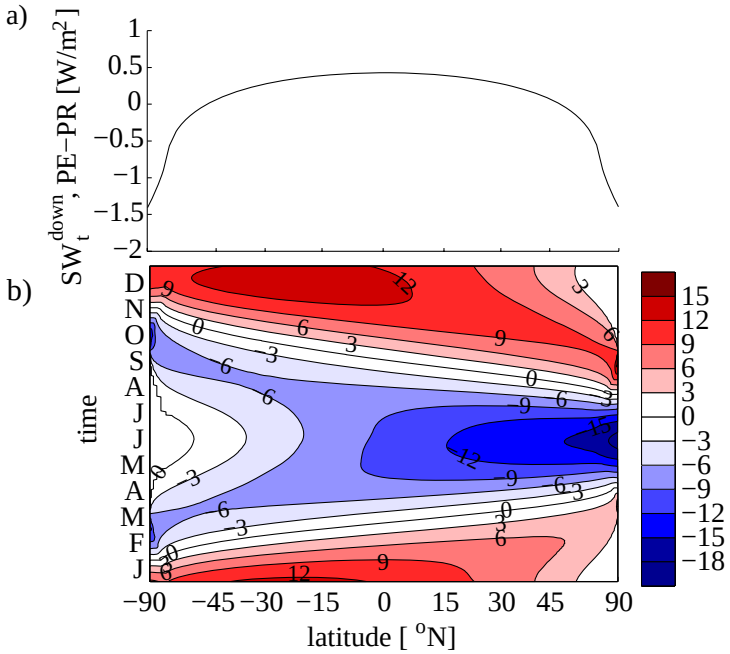


**Fig. 13. (a)** Annual mean and **(b)** seasonal cycle of the difference of the zonal mean incoming shortwave radiation at the top of the atmosphere between PE and PR; red indicates more incoming radiation in the PE simulation. Contour intervals are 3 Wm$^{-2}$. The horizontal scale is linear in the sine of the latitude.